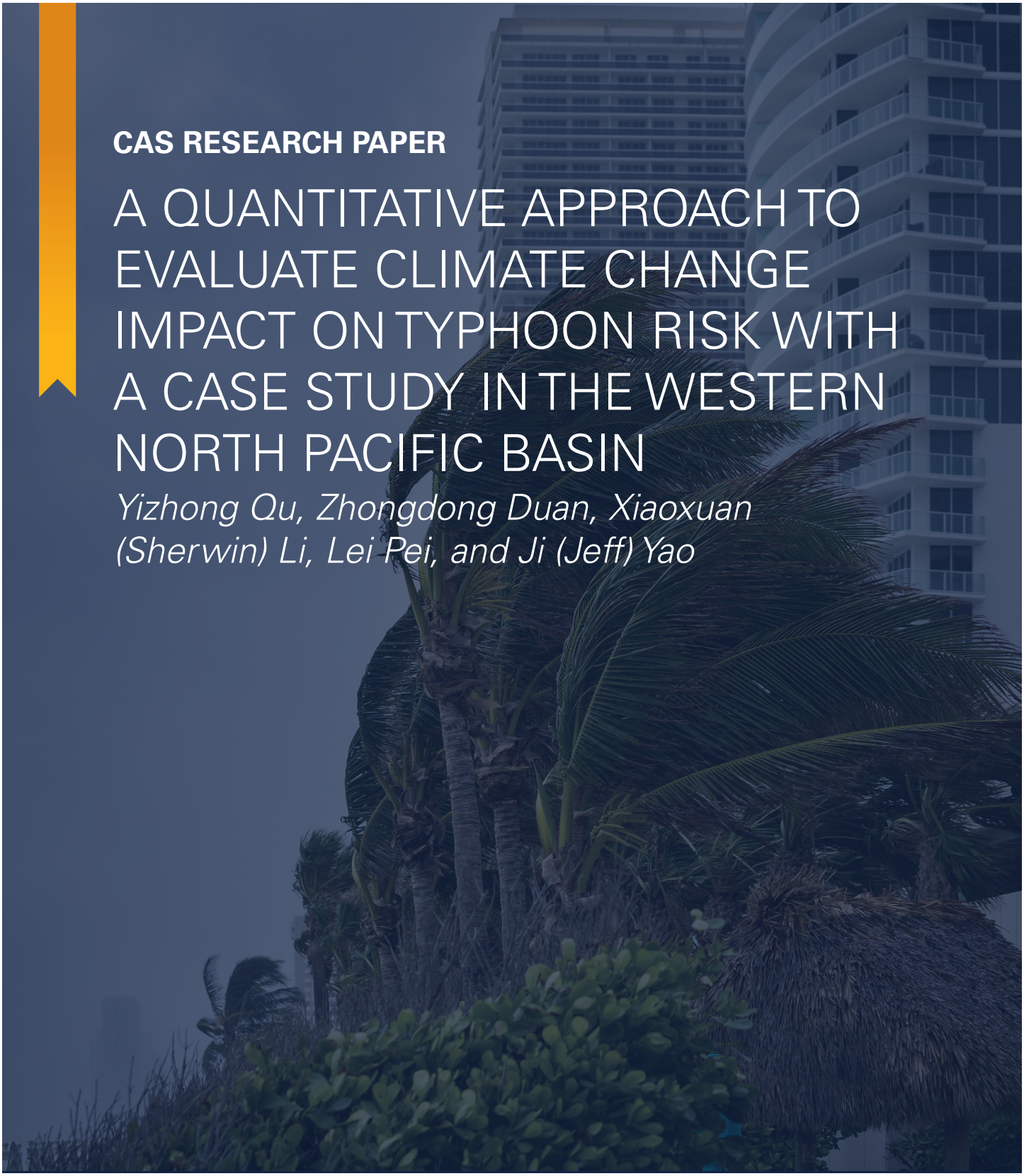

CAS RESEARCH PAPER

A QUANTITATIVE APPROACH TO EVALUATE CLIMATE CHANGE IMPACT ON TYPHOON RISK WITH A CASE STUDY IN THE WESTERN NORTH PACIFIC BASIN

Yizhong Qu, Zhongdong Duan, Xiaoxuan (Sherwin) Li, Lei Pei, and Ji (Jeff) Yao

CASUALTY ACTUARIAL SOCIETY

The Casualty Actuarial Society (CAS) is a leading international organization for credentialing, professional education and research. Founded in 1914, the CAS is the world's only actuarial organization focused exclusively on property-casualty risks and serves over 11,000 members worldwide. CAS members are sought after globally for their insights and ability to apply analytics to solve insurance and risk management problems. As the world's premier P&C actuarial research organization, the CAS reaches practicing actuaries across the globe with thought-leading concepts and solutions. The CAS has been conducting research since its inception. Today, the CAS provides thousands of open-source research papers, including its prestigious publication, *Variance* — all of which advance actuarial science and enhance the P&C insurance industry. Learn more at casact.org.

Caveat and Disclaimer

Contents

A Quantitative Approach to Evaluate Climate Change Impact on Typhoon Risk with a Case Study in the Western North Pacific Basin

Yizhong Qu,[1] Zhongdong Duan,[2] Xiaoxuan (Sherwin) Li,[3] Lei Pei,[4] and Ji (Jeff) Yao[5]

Executive Summary

Climate change is profoundly altering tropical cyclone (TC) activity in the western North Pacific (WNP) basin, with significant implications for typhoon risk in mainland China that might have notable impact on the property and casualty insurance industry, both regionally and globally. This study assesses these changes by employing a quantitative approach to analyzing data from three Coupled Model Intercomparison Project Phase 6 (CMIP6) global climate models (MRI-ESM2-0, BCC-CSM2-MR, and EC-Earth3) under two Shared Socioeconomic Pathway (SSP) scenarios: SSP2-4.5 (intermediate emissions) and SSP5-8.5 (high emissions). We applied a newly developed typhoon detection algorithm to track and analyze TC characteristics, including frequency, intensity, precipitation, and landfall patterns, then integrated the findings into the Verisk mainland China typhoon model to evaluate economic impacts on the insurance industry. This study aims to inform climate adaptation strategies and disaster preparedness for one of the world's most vulnerable regions.

Our study projections indicate a decline in the total number of TCs but an increase in the proportion of high-intensity storms (Categories 4–5), particularly under SSP5-8.5. Typhoon tracks are expected to shift northward, leading to more frequent landfalls in eastern and northern coastal provinces (e.g., Fujian, Zhejiang, and Shanghai). TC-induced precipitation is projected to rise substantially, with southern regions (Hainan, Guangdong, and Guangxi) experiencing the highest increases in the near term, while southeastern China sees a dramatic surge by 2100 under high emissions.

Based on the Verisk mainland China typhoon model, financial risk assessments reveal substantial increases in insured losses, especially for long-return-period events (e.g., 500-year). This trend is largely driven by the rising frequency

[1]Catastrophe and Risk Solutions, Verisk Analytics.
[2]School of Civil and Environmental Engineering, Harbin Institute of Technology (Shenzhen).
[3]Risk Research Institute, PICC Property & Casualty Company Limited.
[4]Risk Management Department, China Pacific Property Insurance Company Limited.
[5]Strategy and Technology Group APAC, AON.

of intense TCs and amplified precipitation, with northern coastal provinces facing disproportionately higher impacts due to track shifts. Sea-level rise further amplifies flood-related losses, particularly in low-lying coastal areas. These findings underscore the need for adaptive risk management strategies in infrastructure planning, insurance pricing, and disaster preparedness to mitigate escalating climate-driven typhoon threats.

In summary, climate change is expected to alter typhoon activity in the WNP basin, with fewer but stronger storms, northward-shifting tracks, and heavier precipitation. These changes pose escalating risks to coastal regions, necessitating robust adaptation measures in infrastructure, insurance, and emergency planning. While this study provides critical insights, limitations include reliance on relatively coarse-resolution CMIP6 data and static vulnerability assumptions. Future work should incorporate higher-resolution models and dynamic exposure adjustments to refine projections. Nevertheless, the results highlight the urgent need for policy and industry action to enhance resilience in one of the world's most typhoon-vulnerable regions.

1. Introduction

Climate change poses a profound and growing threat to the global climate system, with tropical cyclones (TCs) – commonly referred to as typhoons in the western North Pacific (WNP) – among the most significant manifestations of this evolving risk. Typhoons can bring devastating impacts, including extreme winds, heavy precipitation, storm surges, and flooding, which have lasting consequences for the densely populated and economically vital coastal regions of East and Southeast Asia. Understanding how climate change may impact typhoon characteristics, particularly in terms of their track, wind intensity, and precipitation, is a central concern for both scientific research and climate policy. This report investigates how typhoon activity in the WNP basin may change under a warming climate by analyzing data from the Coupled Model Intercomparison Project Phase 6 (CMIP6), a key framework under the Intergovernmental Panel on Climate Change (IPCC), which is the leading international body for the assessment of climate change.

Established in 1988 by the United Nations Environment Programme and the World Meteorological Organization, the IPCC provides comprehensive scientific assessments of climate change risk caused by human activities. Through a series of reports, the IPCC synthesizes the latest climate science findings from thousands of scientists worldwide. One of IPCC's key contributions is its support and coordination of large-scale modeling efforts that simulate the earth's climate system and project its response to anthropogenic forcings (IPCC 2021).

General circulation models (GCMs) are fundamental climate science tools that simulate the physical processes of the atmosphere, ocean, land surface, and cryosphere. These models provide critical insights into the climate system and allow scientists to project future climate conditions under various greenhouse gas emission scenarios (Flato et al. 2013). Given the complexity and variability inherent in the climate system, multimodel ensembles, such as those organized by the Coupled Model Intercomparison Project (CMIP), are particularly valuable for capturing the range of potential future outcomes and uncertainties.

CMIP is a coordinated climate modeling framework managed by the World Climate Research Program. It facilitates standardized climate experiments among modeling groups worldwide, thereby enabling comprehensive model intercomparison and robust climate projections. CMIP6, the sixth phase of this initiative, represents the most recent and advanced set of climate model outputs and forms the scientific foundation for the IPCC Sixth Assessment Report. CMIP6 includes simulations of historical climate (reanalysis) and future scenarios using Shared Socioeconomic Pathways (SSPs), which allow exploration of a wide spectrum of policy and socioeconomic futures. These outputs are instrumental in examining regional and global climate impacts, including changes in extreme weather phenomena like TCs (Eyring et al. 2016). More information about IPCC, CMIP, and SSPs are provided in Appendix B.

Previous studies have conducted similar analyses in other ocean basins using earlier phases of CMIP GCMs. For instance, research focused on the North Atlantic basin using CMIP5 data has indicated a poleward shift in TC tracks and an increased frequency of

intense hurricanes under future warming scenarios (Knutson et al. 2015). Similar trends have been reported in the South Indian Ocean and Eastern Pacific basins, where increases in precipitation rates associated with TCs have been linked to enhanced atmospheric moisture content driven by global warming (Walsh et al. 2016). However, comparatively few studies have focused on the WNP basin, despite the region's critical importance. Even fewer studies have focused on the economic impact, qualitatively or quantitatively, in this region.

Recent literature examining CMIP6 outputs is beginning to reveal important regional distinctions in typhoon responses to climate change. Some studies have suggested that typhoons may become more intense, with a higher proportion reaching Category 4 and 5 status, while other studies have indicated potential shifts in genesis locations and re-curvature patterns (Roberts et al. 2020b). Growing evidence also suggests that climate change could lead to an increase in the rainfall associated with typhoons, primarily due to the Clausius-Clapeyron relationship, which predicts an approximate 7% increase in atmospheric moisture-holding capacity per degree Celsius of warming (Pérez Bello et al. 2022; Trenberth et al. 2003). These findings underscore the need for more detailed regional studies using the latest model outputs.

We applied typhoon tracking algorithms to the gridded outputs of CMIP6 GCMs, extracting storm tracks and relevant intensity parameters. By comparing model-derived storm characteristics under historical and future conditions, we assessed potential changes in track behavior, intensity distributions, and precipitation patterns associated with typhoons. Our approach used typhoon detection algorithms calibrated for coarse-resolution climate models. This involves identifying warm-core, low-pressure systems with coherent wind structures and tracing their trajectories through successive model time steps. Once tracks were established, we extracted and analyzed storm intensity metrics, including maximum sustained wind speeds, minimum central pressures, and total and peak precipitation rates. We then aggregated and statistically analyzed these variables to detect trends and anomalies across different climate scenarios. Particular attention was paid to the SSP2-4.5 (intermediate emissions) and SSP5-8.5 (high emissions) pathways, which bracket a plausible range of future warming.

To validate the CMIP6 model results, we compared the simulated typhoon characteristics under historical scenarios with the best-track data from observational datasets from the China Meteorological Administration (CMA), the Joint Typhoon Warning Center, and the International Best Track Archive for Climate Stewardship. These comparisons allowed us to assess the fidelity of model outputs and apply bias corrections where necessary. The calibrated projections were then used to quantify future changes in typhoon behavior and evaluate the potential impacts on regional climate risks.

This study focused on typhoon activity in the WNP basin, which is the most active TC basin in the world. The study's primary objectives were to: (1) detect and track typhoons from the CMIP6 model outputs under historical and projected climate scenarios; (2) extract and analyze their intensity, including maximum wind speed and precipitation characteristics; (3) compare these characteristics with observational records to quantify the trends; (4) resample the standard 10,000-year stochastic catalog from the widely used Verisk typhoon stochastic catastrophe model to generate a climate change conditioned catalog;

and (5) quantitatively assess changes in industry-insured losses due to climate change using the climate change conditioned catalog.

This report is structured as follows: Section 2 describes the typhoon detection algorithm used on selected CMIP6 models, its validation, and the results. Section 3 presents the statistical trend of typhoon activities derived from climate change scenarios, including projected changes to typhoon tracks, intensities, and precipitation characteristics. Section 4 introduces the existing Verisk mainland China typhoon catastrophe model, which is the primary tool for this numerical experiment. Section 5 focuses on the resampling approach we used to generate the climate change conditioned stochastic catalog based on Verisk's standard 10,000-year catalog in the catastrophe model. Section 6 examines how we developed industry-insured exposure and used it in a case study that quantitatively evaluated the economic impact of climate change on the insurance industry. Finally, Section 7 summarizes the conclusions and outlines recommendations for future research and policy development.

By leveraging the latest generation of climate models and advanced detection algorithms, this study contributes to the growing body of knowledge on climate-induced economic changes in TC activity. Our findings aim to inform regional adaptation strategies, improve disaster preparedness, and support the integration of climate science into coastal resilience planning in one of the world's most vulnerable regions.

2. Typhoon Detection Approach

GCMs, in combination with regional downscaling and TC detection algorithms, are considered the primary approach to projecting future TC activity. With the rapid increase in available computational resources, high-resolution (≤50 km) GCMs have been developed that can resolve TC-like structures, such as warm-core low-pressure systems with associated intense winds (Roberts et al. 2020a). These advancements have allowed researchers to simulate more realistic cyclone features and to study their future characteristics under various climate scenarios.

Several detection and tracking algorithms have been developed to identify TCs within climate model outputs. These methods generally rely on identifying criteria such as closed isobars, vorticity maxima, warm-core structures, and sustained wind thresholds. Pioneering work by Bengtsson et al. (2007), Walsh et al. (2007), and Horn et al. (2014) have established frameworks for detecting and tracking cyclones in coarse-resolution GCMs. More recent studies have refined these methods to improve their performance, especially under changing climate conditions. Hodges et al. (2017), for example, introduced objective feature-tracking techniques to systematically identify cyclonic features across multimodel ensembles.

Recent studies using CMIP5 and CMIP6 data have shown that, although coarse-resolution model results may underestimate TC frequency and intensity, they can still capture robust trends and shifts in TC genesis and track patterns when coupled with effective detection schemes. For instance, Murakami et al. (2014) applied a detection algorithm to multiple GCMs and found consistent projections of increasing intense cyclone frequency in the North Atlantic and Western Pacific. Roberts et al. (2020b) examined CMIP6 models and

found projected increases in global mean TC intensity and poleward migration of the average genesis location. Nakamura et al. (2017) demonstrated the ability of CMIP5 models with detection algorithms to simulate landfall characteristics and interannual variability, particularly when validated against observational data.

The application of such algorithms has yielded important insights in the WNP, the most active TC basin globally. Roberts et al. (2020a) employed high-resolution ensemble modeling with TC tracking and demonstrated that the frequency of high-intensity typhoons is likely to increase, while overall storm frequency may remain stable or decline. Studies by Zhang et al. (2021) and Hatsuzuka et al. (2020) have further highlighted the expected increase in TC precipitation rates, associated with rising sea surface temperatures and enhanced atmospheric moisture capacity per the Clausius-Clapeyron relationship.

2.1. Morphology-Based TC Detection Algorithm Using Gridded Data

This study employed a newly developed scheme for TC detecting and tracking by Wu and Duan (2023). Inspired by identifying closed contours of a TC structure, the algorithm detects coherent vortex signatures in the 850 hPa relative vorticity field and traces their evolution over time. This detection scheme operates in two main stages: identifying candidate TC centers based on morphological characteristics of the vorticity field, followed by temporal linking of these centers to construct entire TC tracks. Below, we summarize the TC detection procedure based on the six-hour data.

The algorithm begins by converting the gridded vorticity data at each six-hour time step into binary images through thresholding, wherein grid points with relative vorticity exceeding a critical value (1.4×10^{-4} s^{-1}) are set to the foreground (value = 1), and others are treated as background (value = 0). Connected component labeling is then applied using a four-neighbor structuring element to group adjacent grid points with vorticity exceeding the threshold into discrete vortex candidates. Only components containing at least 18 connected foreground pixels are retained for further analysis.

To identify the presence of an inner core, each connected region undergoes an erosion operation, which progressively shrinks its boundary. A region is confirmed as a TC seed if (1) the eroded core remains non-empty and (2) the mean 850 hPa relative vorticity within the eroded interior exceeds that along the boundary. The centroid of such a region is recorded as the instantaneous TC center.

Once TC seeds are extracted at each time step, a tracking algorithm links them into continuous trajectories. This is achieved by searching for the nearest seed at the next six-hour interval within a radius of 420 km. Tracks that persist for at least 72 hours and exhibit a path curvature below 0.25 are retained as valid TCs. These criteria help exclude transient mesoscale disturbances and reduce false detections.

The algorithm was validated using the ERA5 (European Centre for Medium-Range Weather Forecasts [ECMWF] fifth generation reanalysis) dataset for 2002–2021 with respect to annual TC frequency, genesis locations, TC passage distribution, translational speed across the WNP basin, and TC landfall location in the China coastal lines, through comparison with the

best-track dataset from the CMA. The method exhibits strong and consistent performance across all validation metrics. It successfully identifies approximately 93% of the observed TCs and achieves an 85% detection rate at the six-hour time-step level. Detailed validation results can be found in Wu and Duan (2023). Beyond its accuracy, the algorithm is also highly efficient, enabling rapid processing of high-resolution, multi-decadal datasets. Given the method's merits and impressive performance, it is expected to project the climatological and interannual variability of TCs in warm climates, as well as the TC footprints and landfall characteristics.

Furthermore, the performance of this method is also benchmarked against two prevailing algorithms, OWZ (Tory et al. 2013) and TRACK (Hodges et al. 2017), using statistics of TC geometric metrics. More details are provided in Appendix A.

2.2. CMIP6 Models Used in This Study

This study used outputs from three GCMs participating in CMIP6. These models were run under two future SSPs: SSP2-4.5 and SSP5-8.5, which represent distinct potential conditions of future climate.

The selected GCMs are as follows:

- **MRI-ESM2-0** from the Meteorological Research Institute (Yukimoto et al. 2019)
- **BCC-CSM2-MR** from the Beijing Climate Center (Wu et al. 2021)
- **EC-Earth3** from the European consortium of national meteorological services and research institutes (Döscher et al. 2022)

Their atmospheric components have horizontal resolutions of $1.125° \times 1.12°$, $1.125° \times 1.12°$, and $0.7° \times 0.7°$ (longitude $\times$ latitude), respectively. Hereafter, these simulations are referred to as MRI, BCC, and EC, and these simulation results are referred to as the GCM model results.

The simulations cover a historical period from 1850 to 2014, driven by observed greenhouse gas concentrations, and future projections of these simulations span from 2015 to 2100 under the specified SSP2-4.5 and SSP5-8.5 forcings.

We chose the models based on careful considerations of (1) data availability for TC detection, (2) extended simulation period with projections for the long-term future (2015–2100), and (3) relatively high resolution within the CMIP6 model ensembles and good performance to effectively simulate WNP tropical cyclones (Han et al. 2021). Although high-resolution datasets ($<$50km, such as $0.25° \times 0.25°$) are available for CMIP6 models, they are limited for the high emission scenario and projected to the middle of this century ($\sim$2050). Therefore, we chose the lower resolution around 1.0° datasets to include two different pathways and long-term projections. We highly recommend that this study be refined when richer high-resolution GCM model results become available.

The historical reference period used in this study was 1985–2014, which spans 30 years. Throughout this report, the term *change* specifically means the difference between a future projection period (30-year window) and this defined historical reference period.

The WNP region for this study is delineated as 0°N–50°N latitude and 100°E–160°E longitude. This specific regional boundary is intentionally narrower than the conventionally defined WNP basin (0°N–60°N, 100°E–180°E). This adjustment was made due to the operational application region of the TC detection method used in this study (Wu and Duan 2023).

To facilitate consistent analysis, all GCM model results were bilinearly interpolated onto a common $1° \times 1°$ grid. Selecting these three models (MRI, BCC, and EC) provides a representative range of physically reasonable estimates for the climatic response of TC activity impacting the WNP within the broader CMIP6 ensembles.

The ensemble mean of the three GCMs was subsequently derived using an equally weighted averaging method. This ensemble mean was then used to construct the climatic targets for the risk analysis.

Table 1 provides a comprehensive list of the climate variables from the GCMs that were used in this study.

The observed TC best-track data are from the CMA tropical cyclone best-track dataset (Lu et al. 2021; Ying et al. 2014) covering the period from 1980 to 2014. This dataset comprises six-hour records of storm positions, maximum wind speed, and minimum central pressure. Landfall and bypass characteristics (i.e., location and central pressure) were determined as follows. For landfalling TCs, the parameters were interpolated from track points intersecting the mainland China coastal boundary. For bypassing TCs (defined as passing within 100 km of the mainland China coastal boundary), the location and central pressure were estimated at the point nearest the coastline.

2.3. Applying the TC Detection Algorithm to Low-Resolution CMIP6 Data

As the spatial resolutions of the selected best available CMIP6 models are generally coarser – approximately $1° \times 1°$ – than the original $0.25° \times 0.25°$ resolution Wu and Duan

Table 1. Descriptions of climate variables in GCMs used in this study.

Variable	Definitions	Frequency	Cell Methods		Unit
			Area	Time	
Ua@850hPa	Eastward wind at 850 hPa	6 hours	mean	point	m s^{-1}
va@850hPa	Northward wind at 850 hPa	6 hours	mean	point	m s^{-1}
rv	Relative vorticity at 850 hPa	6 hours	mean	point	s^{-1}
psl	Sea level pressure	6 hours	mean	point	Pa
pr	Precipitation, liquid and solid phases	3 hours	mean	mean	kg m^{-2} s^{-1}
zos	Sea surface height above geoid	Monthly	mean sea	mean	m
zostoga	Global average thermosteric sea level change	Monthly	mean sea	mean	m

(2023) used for the detection algorithm designed for the ERA5 reanalysis data, adaptations to the method were necessary to ensure its applicability to GCM outputs. Specifically, the first stage of the detection procedure – identifying candidate TC centers based on the vorticity field morphological characteristics – was enhanced using image processing techniques. We applied OpenCV-based methods introduced by Sharma et al. (2021) to perform refined binary segmentation, component labeling, and morphological analysis tailored to coarser-resolution fields. The second stage of the detection algorithm was retained without modification.

To assess the robustness of these modifications, the adapted detection algorithm was tested on ERA5 data that had been bilinearly interpolated to a coarser $1° \times 1°$ grid, thereby emulating the resolution characteristics of CMIP6 models. Validation results confirmed that, even at this reduced resolution, the modified algorithm retained a high detection rate and accurately captured key features of TC activity, including annual TC frequency (Figure 1), genesis (Figure 2), and translation. Therefore, applying the detection scheme to CMIP6 simulations facilitates robust analysis of projected TC behavior across different warming scenarios.

We then applied the enhanced TC detection algorithm to the EC, MRI, and BCC model results. Figure 3 shows the TC tracks our approach detected from their historical datasets landfalling or bypassing mainland China.

Figure 1. The detected annual TC frequency: (a) the annual number of TCs and (b) the error between observed and detected TCs in WNP over the period 2002–2021. Black dotted lines (CMA) indicate TCs in CMA and red lines (O_DET) indicate TCs detected in the ERA5 1° × 1° data. The orange histogram denotes the years that the number of detected TCs was larger than that of the observed, while the blue histogram is the opposite. Note that 2017–2019 data (the shaded area in yellow) were used to tune the method parameters, and the remaining data were used for verification.

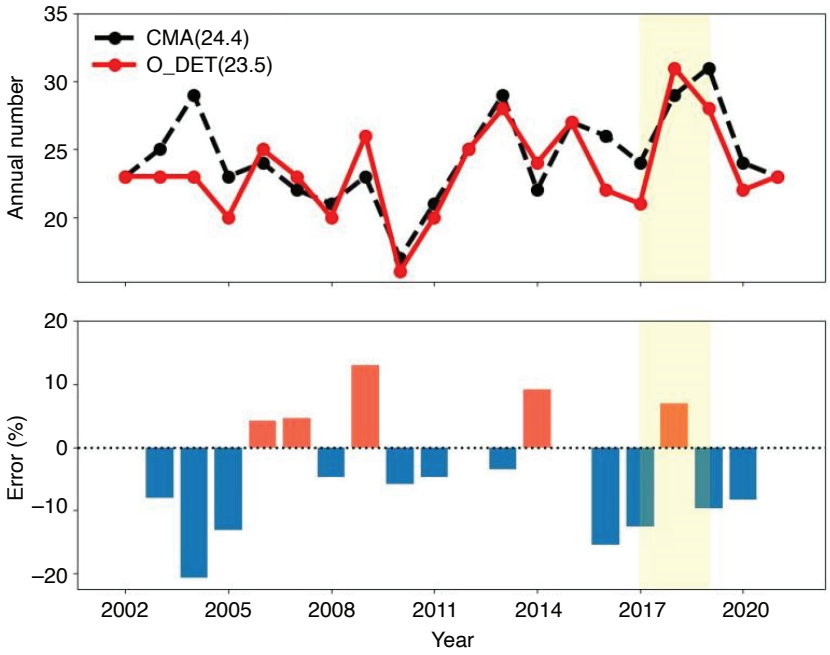

Figure 2. TC genesis locations of observed (CMA) and detected (O_DET) TCs in the WNP, together with kernel density estimation contours (red lines) corresponding to 25%, 50%, 75%, and 100% of the total genesis locations.

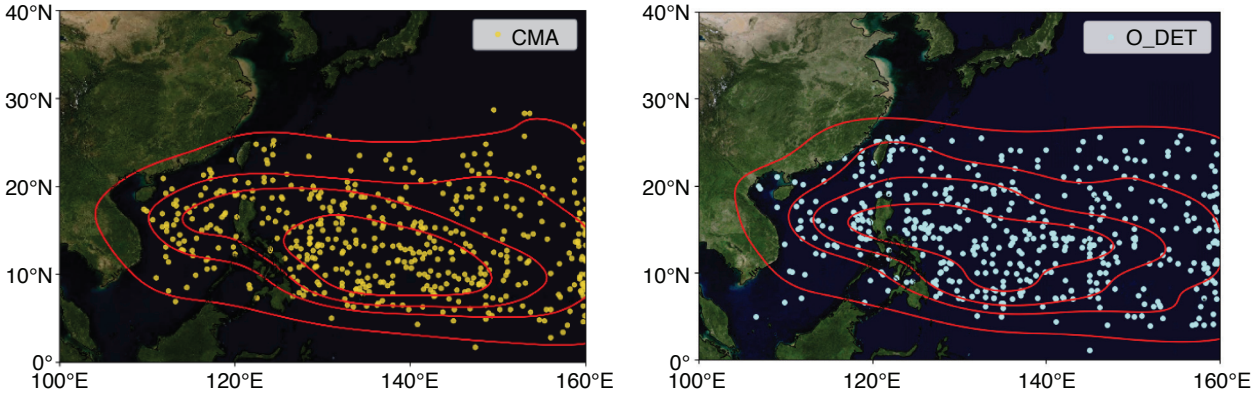

Figure 3. Typhoon tracks detected using our approach from (b) MRI, (c) EC, and (d) BCC historical datasets (1980–2014), compared with (a) CMA best tracks in the same period. The track color is coded by the Saffir-Simpson category of landfall/bypass central pressure. Note that no individual track is identical; however, track statistics are consistent across various datasets.

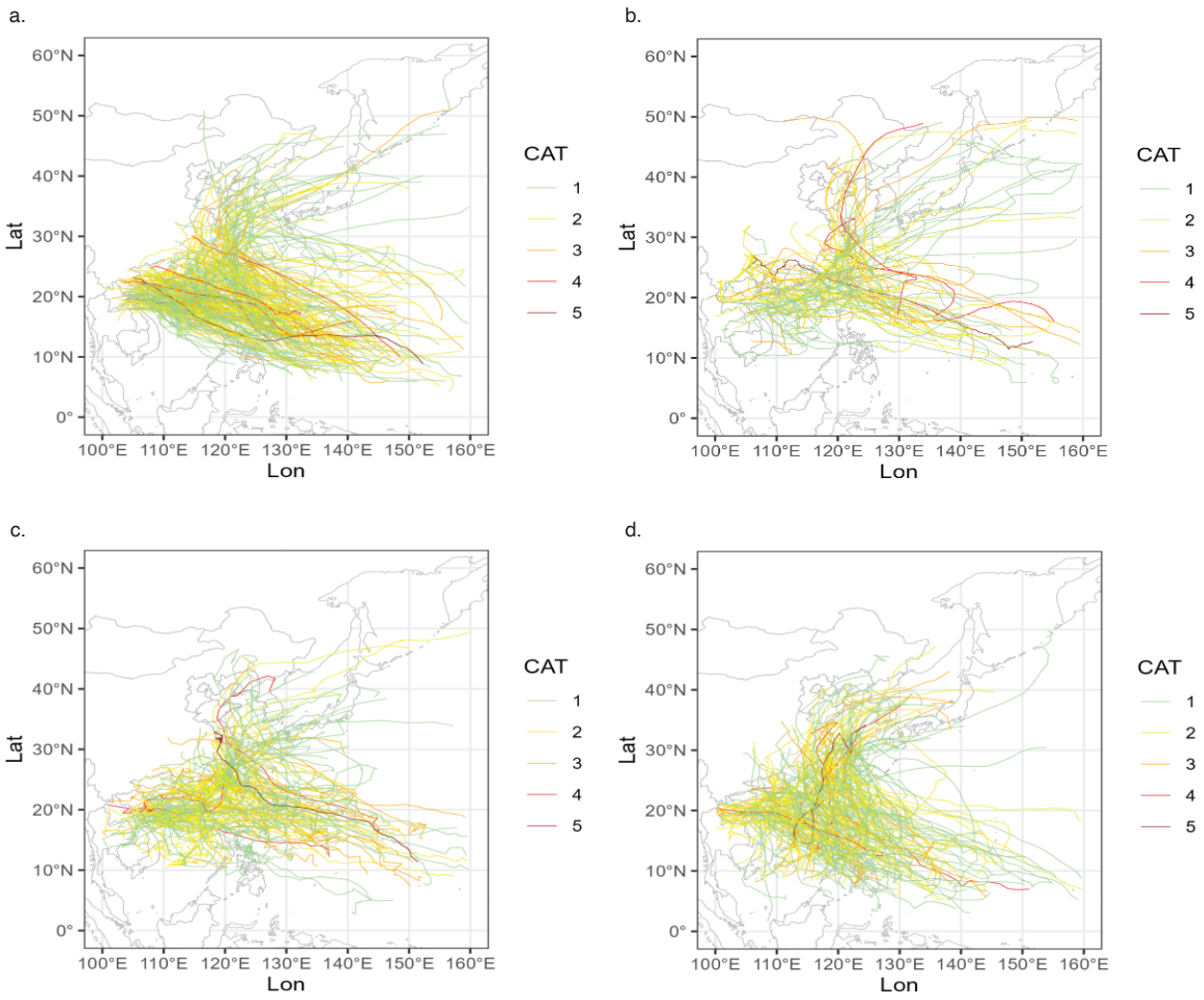

3. Typhoon Activity Trends in Climate Change Scenarios for the WNP Basin

3.1. Overall Observations and Trends

The TC detection algorithm was run on all three GCM model results (BCC, EC, and MRI). Figure 4 shows the trend of annual TC counts for the entire WNP basin in the future scenarios, with mean annual number of TCs in the corresponding periods shown in the legend. A good statistical match for the historical period from 1980 to 2014 shows a clear downward trend in both scenarios based on GCM model results.

At each point along the detected TC tracks, we extracted the intensity variables in Table 1 from the GCM model results to derive a complete set of projected TCs with track and strength parameters. We defined the strength of a typhoon based on the lowest central pressure along its entire trajectory. We observed systematic bias in central pressure from the GCMs compared with the CMA observations (i.e., central pressures from the GCMs were consistently higher than those from the CMA observations). To reconcile this discrepancy, we performed a bias correction by recalibrating the central pressure thresholds used for intensity classification in the GCM data. Specifically, we adjusted the central pressure thresholds for each GCM dataset, using the MRI dataset as an example (see Table 2) to ensure that the resulting distribution of TC intensities statistically matched that of the historical CMA observations. The central pressure from the MRI datasets is the spatial mean of a one-degree grid, while the observed central pressure is typically the point measurement. Given the structure of the typhoon, it is reasonable that the GCM (MRI) central pressure threshold is consistently higher than the CMA observations.

Figure 4. TC activities detected from GCM future model results (MRI, EC, and BCC) for the WNP basin. The triangles represent CMA observations, and crosses depict the average annual TC number from the GCM historical datasets (1980–2014). The squares show the average annual TC number time series from GCM future results in SSP2-4.5, and the diamonds show the time series for SSP5-8.5.

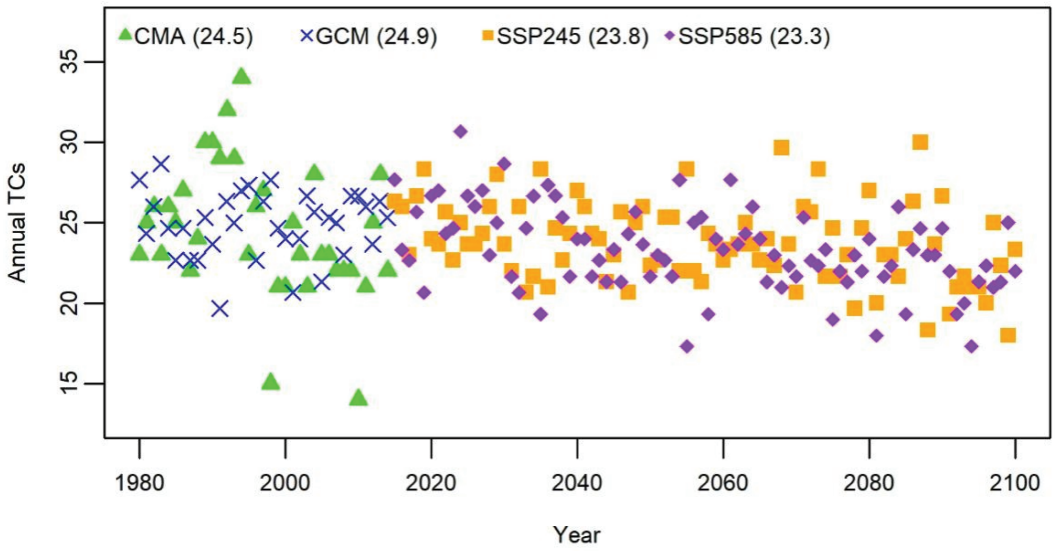

Table 2. Central pressure threshold mapping between MRI datasets and CMA observations for 1980–2014.

Name		Category 1	Category 2	Category 3	Category 4	Category 5
CMA	Central pressure (hPa)	≥980	965–980	945–965	920–945	<920
	Proportion	38.7%	16.2%	22.1%	17.1%	5.9%
MRI	Central pressure (hPa)	≥1,000.0	996.4–1,000.0	989.4–996.4	977.3–989.4	<977.3
	Proportion	38.7%	16.2%	22.0%	17.1%	5.9%

Table 2 details the Saffir-Simpson central pressure thresholds for TCs in the WNP (0–50°N, 100°–160°E), comparing the CMA observational criteria with the newly calibrated thresholds for the MRI model. Each storm is categorized by its lifetime minimum central pressure, and the table shows the resulting percentage of TCs in each category. We conducted similar mapping with EC and BCC, and we found that the calibrated thresholds vary slightly from model to model.

Using the remapped thresholds, we categorized all the typhoons detected from future MRI datasets and listed the strength distribution in Table 3.

While the annual TC numbers in the SSP2-4.5 and SSP5-8.5 scenarios show a decreasing trend, we also observed a shift to stronger TCs in general based on MRI datasets. Also, the EC and BCC model results showed similar but less clear trends. Since no strong evidence emerged to clearly suggest a preferred model, we used the average results from the EC, MRI, and BCC models to conduct further analyses.

3.2. Typhoon Activity Trends for Mainland China

3.2.1. Typhoon Strength Trends

Future projections revealed a discernible trend toward increased landfall/bypass TCs (Figure 5a) and increased TC intensity, which strengthens under higher emission scenarios and progresses over the long-term projection period (Figure 5). By 2050, the distribution of landfall/bypass TC intensity impacting mainland China is anticipated to demonstrate an amplified bimodal pattern. This distribution implies a concurrent increase of both extreme and less intense TCs, alongside a decrease of moderately intense TCs. This finding

Table 3. TC strength distribution in the future scenarios for the MRI dataset.

Scenarios	Period	Category 1	Category 2	Category 3	Category 4	Category 5
SSP2-4.5	2015–2100	32.1%	17.3%	25.2%	18.1%	7.3%
SSP5-8.5	2015–2100	31.7%	15.2%	26.1%	20.0%	7.0%

Figure 5. GCM mean annual landfall/bypass TC statistics for mainland China: a) frequency, and b) percentage distribution by intensity category (CAT_1, CAT_2, CAT_3, CAT_4–5) and total landfall/bypass TCs for historical (1985–2014) and future scenarios (SSP2-4.5, SSP5-8.5) in 2050 and 2100.

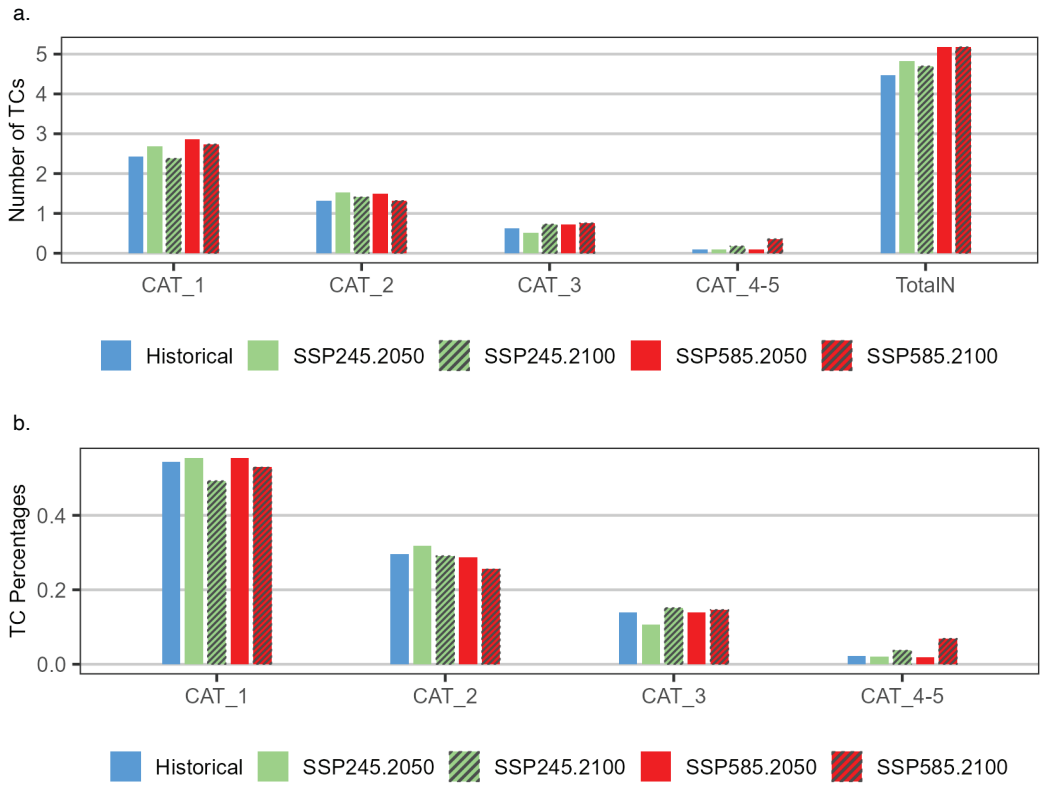

resonates with recent research (Xiang et al. 2025). A potential contributing factor to the increase of less intense TCs is a westward shift in TC genesis, particularly evident during low-intensity phases, and notably for short-lived systems originating in the South China Sea (Zheng and Wang 2023).

3.2.2. Precipitation Considerations

Considering the intensity of TC-induced precipitation, future projections consistently show a general increase in precipitation per track. This trend was observed for all TCs within the WNP basin and specifically for tracks making landfall on or bypassing mainland China (Figure 6). This increase is partly attributable to the principle that warmer air can hold more moisture, leading to heavier rainfall (Qin et al. 2024). The total precipitation along the entire track of TCs generated in the WNP, and the total precipitation over the buffered mainland China region for landfalling/bypassing TCs, were both subjected to our 30-year window averaging and piecewise regression (see Section 5 for more details about window average and piecewise regression). The resulting percentage changes, relative to their historical values, are presented in Figure 6.

Notably, our findings show that TC-induced precipitation will increase more significantly over the ocean than over mainland China. Recent research (Chen et al. 2025) suggests

Figure 6. Projected percentage changes (solid lines) and piecewise regression estimation (dashed lines) of TC-induced precipitation. Total precipitation along the entire track for all WNP TCs (blue and dark blue) and total precipitation on the buffered mainland China for landfalling/bypassing TCs (black and red), under SSP2-4.5 and SSP5-8.5 scenarios. Projected percentage changes mean comparing annual average precipitation per track in 30-year moving windows with the historical base value derived from the 1985–2014 window.

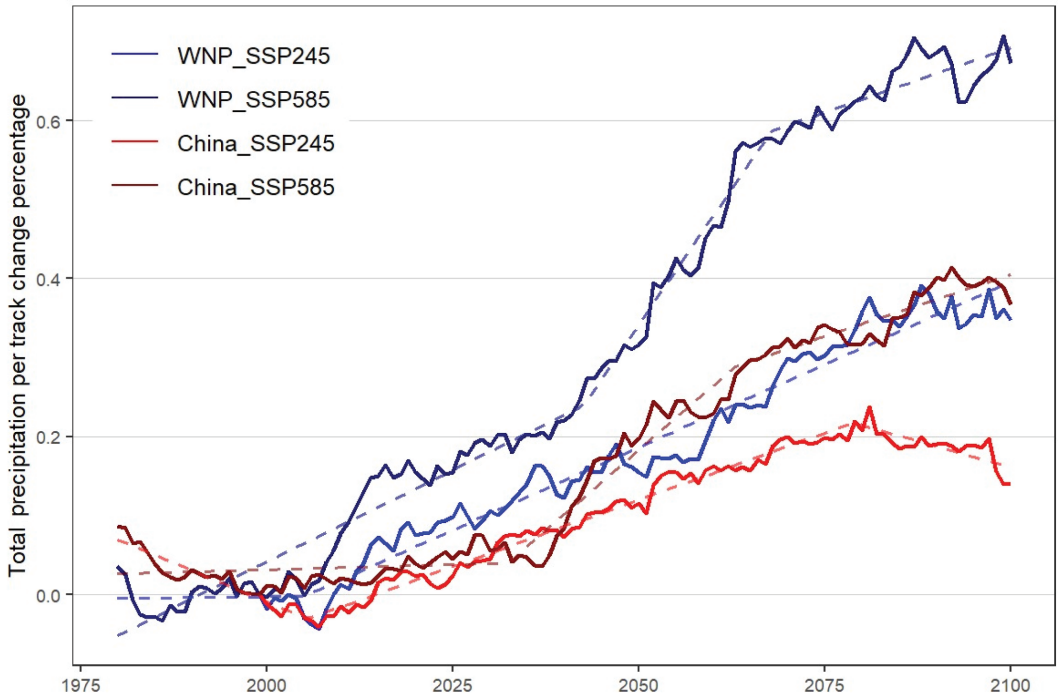

that precipitation within a TC's inner core regions is generally higher over the ocean due to abundant moisture supply from warm ocean waters and stronger updrafts. Conversely, after landfall, the encounter with land surface friction and the loss of oceanic moisture contribute to precipitation decay. Furthermore, in the SSP5-8.5 scenario, TC-induced precipitation is projected to be higher than in SSP2-4.5, which is consistent with the greater warming anticipated under SSP5-8.5.

4. Verisk Mainland China Typhoon Model

The Verisk mainland China typhoon catastrophe model is widely used in the insurance industry because it projects risk from both wind and precipitation-induced floods, which are perils covered by standard residential, commercial, and construction all risks/erection all risks policies. The model accounts for the geographic and meteorological factors that influence precipitation and typhoon-induced flooding, including (1) coastal mountains that enhance precipitation on the north side of typhoons approaching the mainland; (2) the annual South China Sea monsoon, which pumps tropical moisture northward across China's southeastern provinces in summer and fall; and (3) extratropical cyclone transition, which can rejuvenate precipitation after landfall. The flood module is a gridded rainfall-runoff-routing hydrologic model that, cell by cell, simulates excessive runoff from

precipitation based on land use and land cover data with normal antecedent condition and calculates an event flood index at each cell, which is essentially event flow accumulation normalized by its contributing area.

The model's stochastic catalog was developed in conjunction with the Shanghai Typhoon Institute, whose typhoon track data are consistent with the CMA datasets but extend well beyond the point where the storm is no longer a typhoon – long after other meteorological organizations stop tracking it. This information is essential for accurately modeling the flood risk associated with these systems.

Verisk engineers collaborated with the Beijing Institute of Architectural Design to better understand local building designs and construction materials and practices. The model includes separate damage functions for wind and flood, which capture the relationship between wind speed or flood index and the vulnerability of affected structures, accounting for related factors such as height, construction, and occupancy. The damage functions also account for wind and rain duration. The Verisk China typhoon model's damage functions incorporate the results of engineering research and damage surveys and have been validated using actual losses from several typhoons, including Fitow (2013), Rammasun (2014), Mujigae (2015), and Meranti (2016).

To produce realistic and robust model results, Verisk builds its models from the ground up, validating each component independently against multiple sources. Verisk modeled wind speeds from the Japan Meteorological Agency and validated precipitation totals using data from the Shanghai Typhoon Institute of China Meteorological Administration Tropical Cyclone Yearbooks and from NASA's Tropical Rainfall Measuring Mission (TRMM) and Global Precipitation Measurement Mission (GPM) satellite products.

Verisk also validates from the top down, comparing modeled losses with industry loss estimates and company data. Modeled losses for the Verisk typhoon model for China were validated against actual major typhoon loss and claims data since 2004, from companies representing 60%–70% of China's total premium. Verisk's comprehensive approach to validation confirms that overall losses are reasonable and that the final model output is consistent with both basic physical expectations of the underlying hazard and unbiased when tested against historical and real-time information.

The Verisk typhoon model for China supports a wide array of policy terms and conditions, including location limits and deductibles, policy limits and deductibles, and facultative (assumed and ceded) and treaty reinsurances. In addition, the model explicitly includes the maximum of site or percent-of-loss deductible type, a commercial policy condition commonly used in China's insurance market (see Table 4).

The purpose of this study was to resample from the 10,000-year catalog of the Verisk typhoon model for mainland China based on the changes estimated from previous sessions to form a climate-conditioned catalog, then run it against the Verisk industry-insured exposure datasets to evaluate the financial impact.

Table 4. The Verisk typhoon model for China at a glance.

Aspects	Description
Model perils	Tropical cyclone winds and precipitation-induced flood.
Stochastic catalog	10,000-year catalog includes 294,206 simulated events. Nine historical events are also included.
Geographic resolution	Touchstone Re: province, county.
	Touchstone: province, county and postcode resolution, plus user-provided latitude and longitude.
Construction classes and occupancies	18 construction classes are supported for wind and precipitation-induced flood.
	52 occupancy classes are supported for wind and precipitation-induced flood.
Policy conditions	The model supports a wide variety of location, policy, and reinsurance conditions, as well as the maximum of site or percent-of-loss deductible type.

5. Climate-Conditioned Catalog Generation

5.1. TC Track Classification

WNP TCs are commonly categorized by their track geometry (Colbert et al. 2015; Shan and Yu 2021) or by a multivariate approach encompassing lifespan, wind speed, frequency, power dissipation index, and spatial rainfall distribution (Yan et al. 2025). To evaluate the potential implications of climate change for typhoon-related property insurance risk within the WNP, this study classified WNP TC tracks according to their proximity and impact on predefined threatened regions, with a primary emphasis on mainland China.

A landfall is operationally defined as a detected TC whose grid center intersects any segment of the coastline. A bypass is defined as a detected TC maintaining a minimum distance from the coastline of less than or equal to 100 km. In instances of multiple landfalls by a single TC, only the initial landfall is recorded.

In this study, WNP TC tracks are conventionally categorized into three distinct types:

- **Type 1:** Includes TCs with a westward trajectory that either traverse the Philippines or originate in the South China Sea, without subsequently impacting mainland China.
- **Type 2:** Encompasses TCs that make landfall on or execute a bypass maneuver relative to mainland China.
- **Type 3:** Represents recurving tracks that proceed toward the Korean Peninsula, Japan, and the broader Pacific Ocean.

Figure 7. TC track classification zones and mainland China coastal regions of threat.

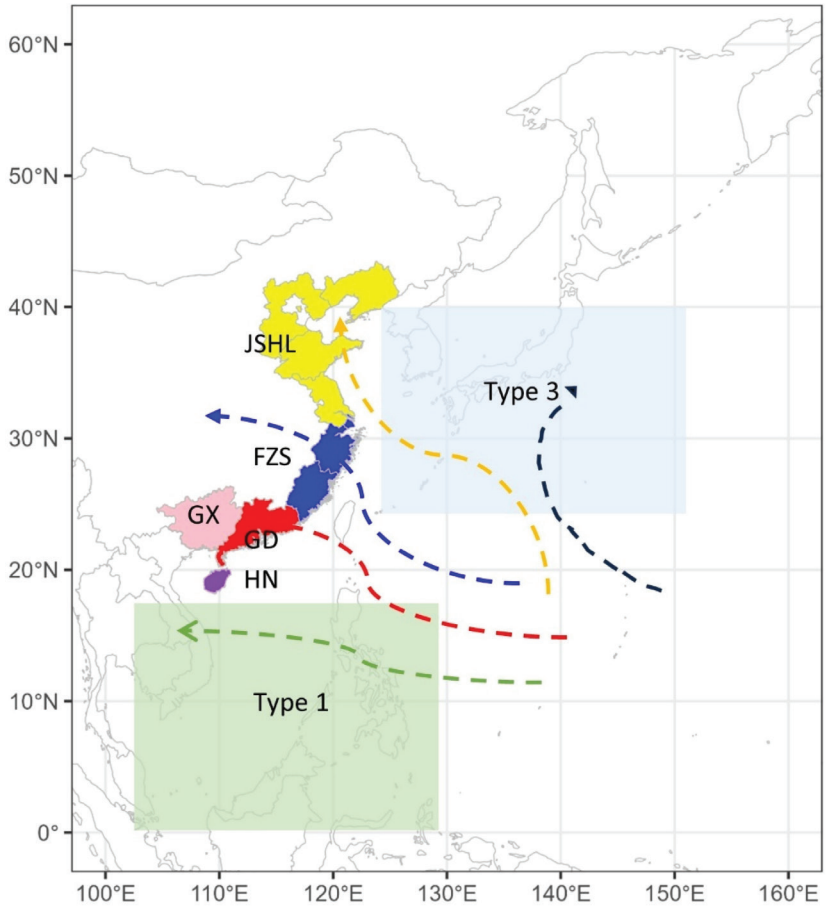

To facilitate a more granular assessment of climate change's influence on WNP TCs affecting mainland China, Type 2 tracks are further refined by categorizing the country's coastal regions into the following geographical divisions (Figure 7):

- **HN:** Hainan Province
- **GX:** Guangxi Province
- **GD:** Guangdong Province
- **FZS:** Fujian and Zhejiang Provinces, and Shanghai City
- **JSHL:** Jiangsu, Shandong, Hebei, and Liaoning Provinces

We used our algorithm to determine the track classification for each typhoon in the CMA historical, GCM historical and future, and Verisk 10,000-year stochastic events conditions.

5.2. Northward TC Tracks and Northward Landfall/Bypass Locations Along the Mainland China Coastline

In analyzing track classifications, this study focused on relative percentage changes rather than absolute changes. We adopted this approach to reduce sensitivity to the TC detection

scheme and to highlight trends. Table 5 presents the TC percentages for each track classification type across the three GCMs for both the historical and two future scenarios, facilitating comparisons of future projections against their corresponding historical periods.

Comparing the tracks, significantly fewer Type 1 TCs (those primarily affecting Vietnam, the Philippines, and the surrounding sea) are projected in future scenarios, likely attributable to a poleward movement of genesis trends.

Conversely, for the mainland China landfall/bypass types under SSP2-4.5 and SSP5-8.5, FZS and JSHL types (affecting southeast, east, and north China) show a proportionally greater increase in TC occurrence than the GD, GX, and HN types (southern coastal regions). This suggests a northward shift in TC activity impacting the Chinese mainland.

To facilitate a more robust comparison of track geometry and landfall/bypass locations, we analyzed TC tracks from the three GCMs (MRI, EC, and BCC) by aggregating their initial 10-day segments (i.e., averaging latitude and longitude of six-hour track locations over all tracks for each of the three GCMs over the first 10 days). See Figure 8. This aggregation was performed for all WNP tracks and specifically for tracks making landfall on or bypassing mainland China, covering the historical period, 2050, and 2100.

A prominent finding from this analysis is a general northward shift in the trajectory of WNP TCs, where red tracks (SSP2-4.5) and green tracks (SSP5-8.5) are north of the black tracks (historical), and tracks in dense colors (dark red for SSP2-4.5 in 2100, dark green for SSP5-8.5 in 2100) are north of the tracks in light color (red for SSP2-4.5 in 2050, green for SSP5-8.5 in 2050). See Figure 8 a–c. This shift is particularly evident in the MRI and EC models and reaches its highest significance under the SSP5-8.5 scenario by 2100.

Table 5. Percentage of total TCs within each track classification type.

Model.Period	GD	GX	HN	FZS	JSHL	Type 1	Type 3	Others
MRI.historical	4%	0.0%	3%	5%	0.3%	15%	51%	22%
EC.historical	4%	0.5%	5%	8%	1%	19%	43%	19%
BCC.historical	8%	0.5%	5%	9%	0%	22%	42%	13%
MRI.SSP2-4.5	4%	0.1%	3%	6%	1%	13%	52%	20%
MRI.SSP5-8.5	4%	0.3%	3%	6%	1%	13%	53%	18%
EC.SSP2-4.5	5%	0.5%	5%	10%	1%	20%	38%	20%
EC.SSP5-8.5	6%	0.5%	7%	10%	1%	17%	40%	18%
BCC.SSP2-4.5	9%	0.2%	5%	8%	0.4%	20%	42%	15%
BCC.SSP5-8.5	9%	0.5%	6%	10%	1%	18%	41%	14%

Note: Data presented for three GCMs under the historical period (1985–2014) and future SSP2-4.5 and SSP5-8.5 scenarios (2015–2100).

Figure 8. Aggregated initial 10-day TC tracks. Panel a–c: all WNP TCs; panel d–f: TCs making landfall on or bypassing mainland China, derived from MRI, EC, and BCC GCMs for the historical period, 2050, and 2100.

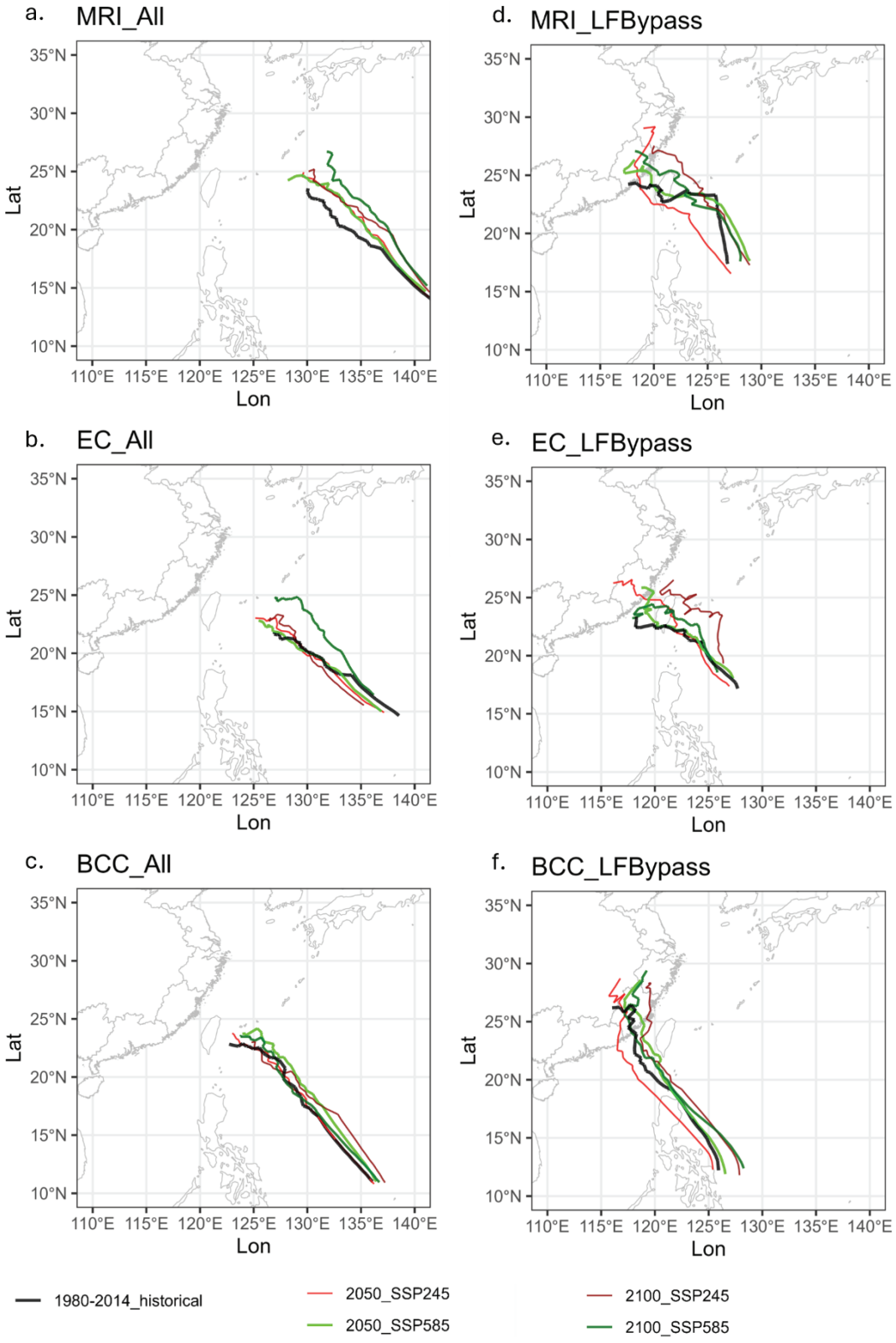

Concurrently, the mean TC landfall point along the mainland China coastline is projected to move northward (Figure 8 d–f), with this shift becoming more pronounced in the long-term future (2100).

5.3. TC Intensity Category and Bias Correction

TC intensity or strength (defined by central pressure and precipitation) for each classification type are determined by extracting its intensity parameters from its CMIP6 GCM model results. These estimations cover both the historical scenario (1980–2014) and future scenarios (SSP2-4.5 and SSP5-8.5 for 2015–2100).

As described in earlier analyses, we employed an intensity category mapping method to address systematic biases in TC intensity estimates, primarily caused by the coarse resolution of GCMs (≈ 100 km $\times$ 100 km grid area mean). This bias correction method maps the intensity category of a detected TC in the GCM to that of an observed TC, ensuring they share the same probability in the cumulative distribution function of the central pressure. Adjustments were calculated using observations from the CMA best tracks.

The intensity categories were then mapped to the five Saffir-Simpson categories. For tracks making landfall on or bypassing mainland China (i.e., classification types HN, GX, GD, FZS, and JSHL), this mapping uses historically detected TCs and CMA best tracks based on landfall/bypass central pressure (similar to the mapping method shown in Table 2). For classification Types 1 and 3, intensity categories were estimated based on the minimum central pressure of GCM-detected TCs and CMA best tracks during the historical period.

While robust, this bias correction method has limitations that warrant consideration when assessing TC intensities. First, the method is statistical rather than dynamical; therefore, it does not account for nonlinear responses and assumes that the relationships driving the bias correction remain constant under evolving climate change conditions. Second, the method requires sufficient observational information to yield reliable results. Despite these shortcomings, this bias correction method is considered the most reliable approach for mitigating the limitations arising from insufficient model resolution (Liu et al. 2024).

5.4. TC Precipitation Consideration

Investigating TC-induced precipitation under climate change presents significant challenges due to the complex characteristics of precipitation that drive losses, including peak volume, the timing of peak precipitation (Zhai et al. 2024), seasonal patterns (Shan et al. 2023), and related changes in hydrologic processes (Lai et al. 2024).

In the Verisk typhoon modeling framework, TC-induced precipitation is modeled based on the precipitation characteristics along the track and its localized intensity within the modeling area. For this study, we only analyzed total precipitation induced by TCs. This is defined over mainland China and a 400-km buffer zone along its coastline for the HN, GX, GD, FZS, and JSHL classification types. For Types 1 and 3, we considered the total precipitation along the entire track within the WNP. The detailed precipitation characteristics were subsequently captured by the Verisk model through resampling TC events from the Verisk typhoon event catalog, guided by the total precipitation change target.

Table 6. Projected percentage change in TC-induced precipitation per track-by-track classification types (HN+GX+GD, FZS, JSHL) across SSP2-4.5 and SSP5-8.5 scenarios in 2050 and 2100.

	SSP2-4.5		SSP5-8.5	
Classification Types	**2050**	**2100**	**2050**	**2100**
China Mainland	12%	16%	18%	41%
HN+GD+GX	17%	26%	28%	23%
FZS	12%	6%	9%	78%
JSHL	–16%	6%	1%	–2%

Future projections indicate that TC-induced precipitation exhibits spatial variations along the mainland China coastline. Table 6 shows the piecewise regression estimated TC-induced precipitation change percentages by classifications, combining HN, GD, and GX as HN+GD+GX for the southern provinces and combining HN, GD, GX, FZS, and JSHL as China mainland for all the mainland China coastline. Specifically, TCs making landfall on or bypassing the southern provinces (HN, GX, GD) were projected to induce greater precipitation compared with those impacting the southeast, east, and north China regions (FZS, JSHL). This general pattern, however, shows a notable exception. Under the SSP5-8.5 scenario by 2100, the southeastern provinces (FZS) experience a significant increase in TC-induced precipitation. The increasing trend of TC-induced precipitation in southern China may be closely related to sufficient water vapor supply and an increase in average duration and intensity of TCs after landfall (Liu and Wang 2020).

5.5. Resampling Approach to Generate Climate-Conditioned Catalog

5.5.1. Analysis of Typhoon Activity Characteristic Changes

This study explored changes in typhoon activity characteristics under the SSP2-4.5 and SSP5-8.5 future scenarios for the three GCMs. This exploration was based on the following:

1. **TC frequency:** Analyzed by combinations of intensity categories (Category 1, Category 2, Category 3, and Categories 4–5) and track classification types (HN, GX, GD, FZS, JSHL; Type 1 and Type 3).
2. **Total precipitation volume:** Analyzed by track classification types.

Annual TC frequency and annual average precipitation per track were calculated using a 30-year moving window method. We then estimated the percentage changes for these variables by comparing them against a historical base value derived from the 1985–2014 window. The mean change percentages across the three GCMs were calculated with equal weighting for each GCM, except that the BCC model was excluded from precipitation change percentage estimations due to an inconsistency observed between its historical and future simulated precipitation.

Piecewise linear regression was applied to regress each window-averaged typhoon variable (e.g., the change percentage of TCs making landfall on or bypassing Guangdong [GD] with a central pressure corresponding to Saffir-Simpson Category 3). We performed this regression for the period 1980–2100, allowing for at most two change points. Detecting change points in weather variables commonly assumes at most one change point. To avoid the pitfalls of oversimplification and overfitting, this study assumed at most two change points. We used the Bayesian information criterion, which tends to penalize complexity more heavily than the Akaike information criterion, to select the optimal model among linear regression, one-point piecewise linear regression, and two-point piecewise linear regression.

The estimated values for 2050 and 2100, derived from these regression models, were chosen to represent future TC statistics. These values also served as the target variables for subsequent resampling procedures.

5.5.2. Resampling of Stochastic Event Catalogs

As mentioned earlier, the Verisk mainland China typhoon model has been validated and widely used in the region. We used Verisk's 10,000-year stochastic event catalog and resampled it based on the future TC statistics estimated from our climate change projections. This process, leveraging Verisk's frequency adjustment feature, yielded a climate-change-conditioned typhoon catalog for the region, ready for portfolio analysis.

The resampling process proceeded as follows:

1. **Event labeling:** Each event within the Verisk stochastic catalog was first labeled with its corresponding classification type, intensity category, and total precipitation. As previously defined, the intensity category and total precipitation were assigned based on the classification type.
2. **Target statistic estimation:** Target TC frequencies for each combination of classification type and intensity category were derived from our regression models' estimated TC statistics (e.g., an increase of 20%). Similarly, target precipitation per track was estimated based on the projected TC statistics (e.g., an increase of 15%).
3. **Resampling execution:** Resampling was then conducted using these estimated TC frequencies and target precipitation per track.

Specifically, this study resampled a new 10,000-year climate change-conditioned catalog from the Verisk 10,000-year stochastic catalog for each combination of the two future scenarios (SSP2-4.5 and SSP5-8.5) and two projection years (2050 and 2100).

6. Case Study

6.1. Industry-Insured Exposure Development

A key asset of the Verisk typhoon model for mainland China is the Verisk industry-insured exposure dataset, which depicts the risk counts for all lines of business and replacement values. This dataset was derived from numerous publicly available data sources, including

the National Bureau of Statistics of China, the China Statistical Yearbooks, county-level census data, and the China insurance industry yearbook. Census data were used to determine establishment counts in various business catalogs, numbers of employees in various business sectors, household and population counts, and average household living area. Estimates of risk counts for different lines of business were updated using annual information on population increases, number of households, and projects under construction. Property replacement values were estimated at the county level using statistical data and per household living-area census data, statistical data on building space (area) for industrial use, and per unit construction costs for buildings of various construction types. County-level exposure was then distributed to a 5 km × 5 km grid based on population density data, land use and land cover data, and satellite images.

Figure 9 shows the sum insured value (or replacement value) data for commercial and industry lines in Verisk's insured exposure dataset, recalibrated using industry-insured data from the 2024 China insurance industry yearbook. We used these data to evaluate the economic impact of typhoon activity changes related to climate change scenarios.

6.2. Sea-Level Rise Consideration

Global mean sea-level change results from both ocean density changes caused by thermal expansion of water due to warming oceans (thermosteric sea-level change) and the exchange of mass between the ocean and cryosphere or land (barystatic sea-level change), resulting in increased ocean volume.

Figure 9. 2024 industry sum insured value by province for commercial and industrial lines.

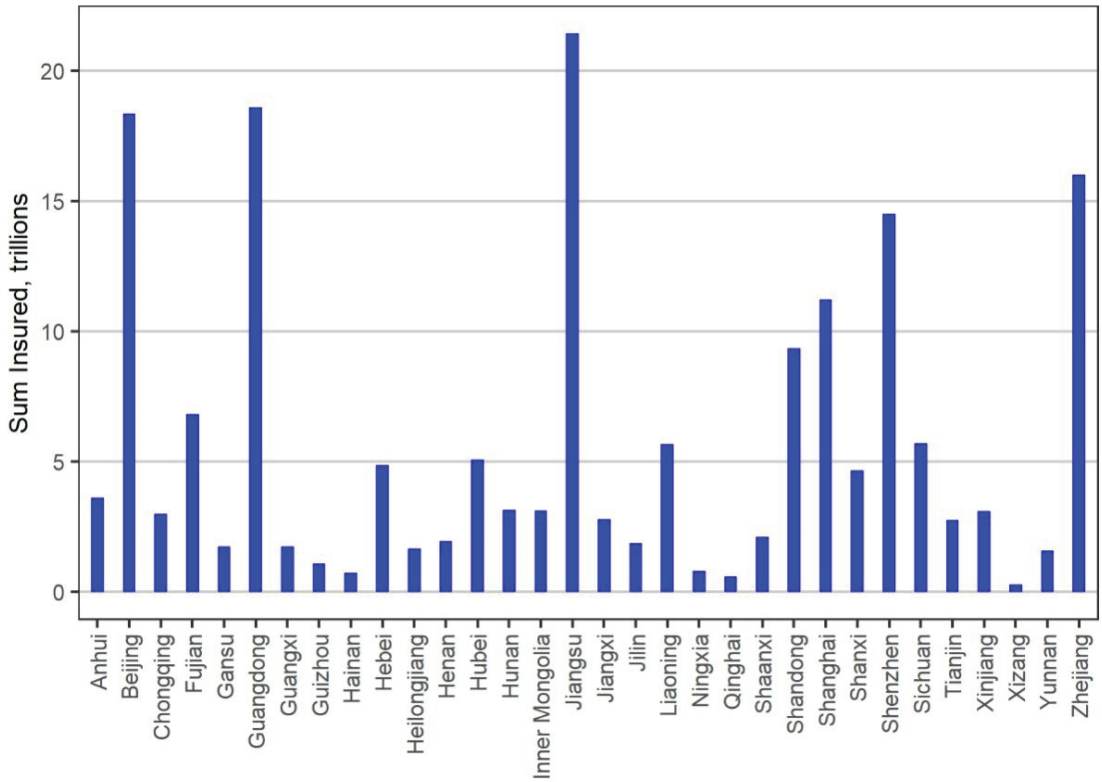

The CMIP6 Data Request defines the variables requested from each experiment and specifies the time intervals for which they are supposed to be reported. In the Data Request, global average sea-level change data are not listed and global average thermosteric sea-level change data (zostoga) are listed as optional, therefore many CMIP6 experiments generally do not include mature interactive and evolving land glacier and ice sheet models (Durack 2015). Of the three GCMs used in the study, only EC-Earth3 has both monthly zostoga and zos (sea surface height above geoid) data available to derive sea-level rise along the mainland China coastline.

A simplified sea-level rise estimation (Kim et al. 2021) is calculated as Equations (1) and (2):

$$SLR(x,y,t) = \Delta SSH(x,y,t) = SSH(x,y,t) - SSH(x,y,2014), \text{ and} \tag{1}$$

$$SSH(x,y,t) = zos(x,y,t) - zos_{m(t)} + zostoga(t) + bary_{sle(t)}, \tag{2}$$

where the sea surface height (SSH) above the geoid (zos) is the dynamic sea level reflecting fluctuations from the geoid. The global mean sea surface height (zos_m) was removed from zos to exclude spurious model drift in each GCM. Global mean sea level change due to thermosteric effects (zostoga) and the correlated change in ocean mass (i.e., mass effect and bary_sle) were then added. As mentioned, only zostoga is directly available in the CMIP6 dataset; therefore, this study assumed global average thermosteric sea-level change accounts for 39.4% of the total global average sea-level changes based on the recent data (NASA n.d.; i.e., zostoga = 39.4% ∗ [zostoga + bary_sle]). The sea-level rise estimation is summarized in Table 7 for SSP2-4.5 and SSP5-8.5 in 2050 and 2100.

Jin et al. (2021) also analyzed sea-level rise along the China coast under climate change scenarios. The authors estimated that sea-level rise of nearshore China would be 0.22 meter (0.19 ~ 0.28 m) and 0.24 meter (0.21 ~ 0.33 m) in 2050, and 0.59 meter (0.47 ~ 0.8 m) and 0.83 meter (0.64 ~ 1.09 m) in 2100, for SSP2-4.5 and SSP5-8.5, respectively, which is similar to our estimation in Table 7.

Although the sea-level rise is in the sub-meter range, it would cause more damage because it is the baseline of the storm surge and coastal flood. However, the Verisk mainland China typhoon model does not allow users to explicitly change the mean sea level.

Table 7. Sea-level rise (in meters) used in this study for various climate change scenarios.

Sea-Level Rise	SSP2-4.5	SSP5-8.5
2050	0.22	0.28
2100	0.58	0.91

Table 8. Loss modification factor (LMF) derived from sea-level rise study and used in this study.

LMF to Loss	SSP2-4.5	SSP5-8.5
2050	1.03	1.04
2100	1.07	1.10

Therefore, we conducted a separate study to lower ground elevation by the same amount to simulate the impact of sea-level rise on the vulnerability of commercial/industry line of business in the research version of the stochastic catastrophe model. The study used the custom elevation feature in Verisk's model to override the default underlying modeled digital terrain elevation. The loss modification factor was derived by dividing the loss based on the custom elevation considering sea-level rise by the loss using the default modeled digital terrain. Table 8 summarizes the average loss increase due to sea-level rise. These factors were correspondingly applied in our stochastic simulation for the counties along the coastal line.

6.3. Results and Discussion

To assess the future impacts of climate change, the standard 10,000-year stochastic catalog was resampled to align with both wind and TC-induced precipitation targets for the SSP2-4.5 and SSP5-8.5 scenarios in 2050 and 2100. A loss estimation simulation was then run on this climate-conditioned event set using an industry-standard insurance exposure database, with results adjusted by loss modification factors to account for sea-level rise.

The analysis compares losses from these climate-conditioned catalogs against the standard Verisk catalog to quantify the impact of climate change on typhoon losses. Figures 10a and 10b show the country's aggregate and occurrence average annual loss alongside losses at 5-, 10-, 100-, and 500-year return periods. For comparison, all losses are standardized by the aggregate loss at the 500-year return period for the SSP5-8.5 scenario in 2100. The corresponding percentage changes in these metrics are detailed in Tables 9 and 10.

6.3.1. Key Drivers of Increased Losses

A key finding for simulation year 2100 was that losses at longer return periods (e.g., 500-year) increase more significantly than losses at shorter return periods under both climate scenarios. This trend is driven by a projected rise in the frequency of intense Category 4 and 5 TCs, which outweighs the shifts in lower-category storms. As shown in Figure 5, the frequency of Category 1 TCs is actually projected to decrease under the SSP2-4.5 scenario in 2100.

Increased precipitation is another major contributor to higher projected losses across all return periods, particularly in 2100. For example, under SSP2-4.5, TC-induced precipitation is expected to increase by 26% in Hainan, Guangdong, and Guangxi and by a notable 78% in Fujian, Zhejiang, and Shanghai under SSP5-8.5 (Table 6).

Figure 10. a. Aggregate loss; b. Occurrence loss increases in SSP2-4.5 and SSP5-8.5 compared with the current climate condition.

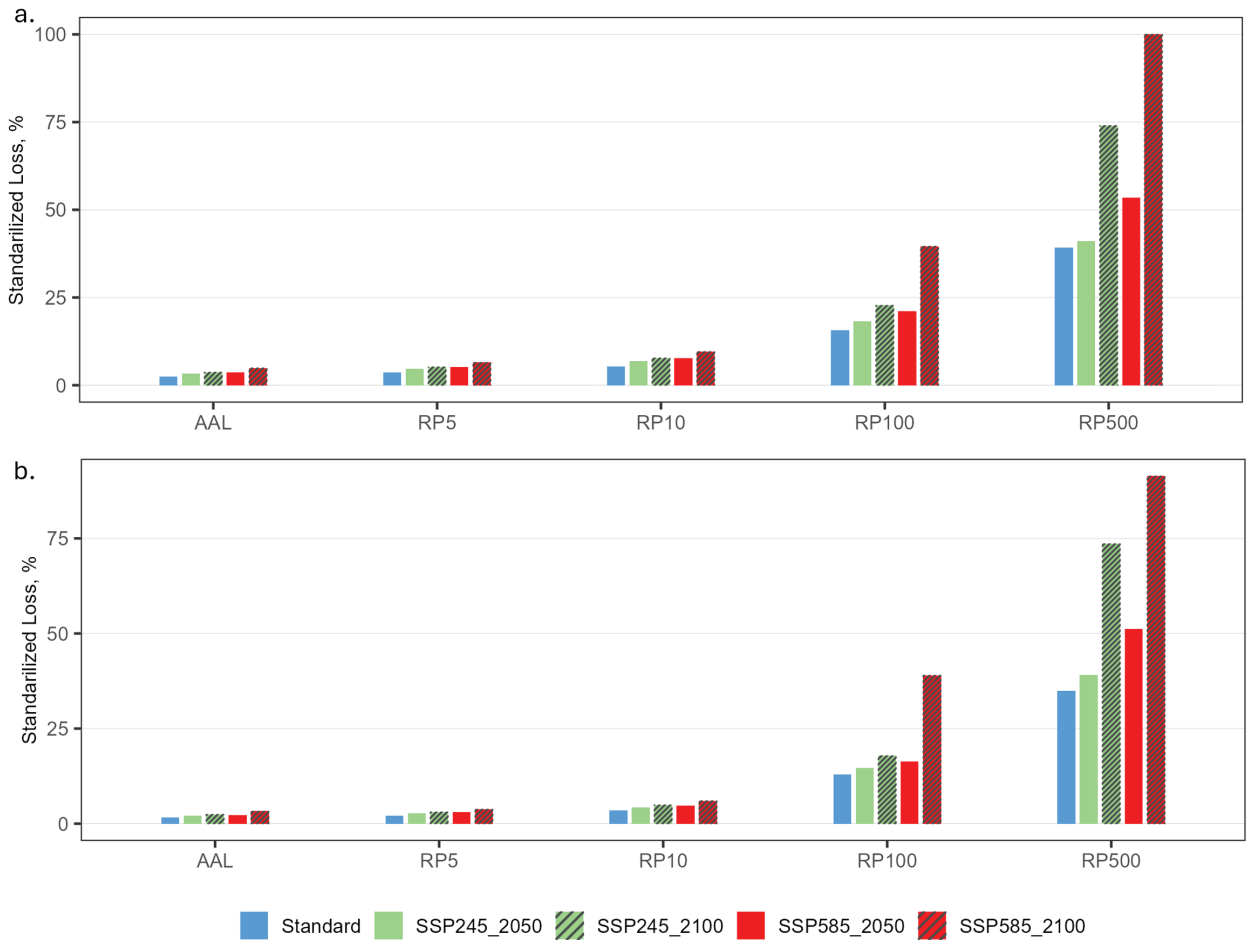

Table 9. Aggregate loss increases in percentage.

	AAL	RP 5	RP 10	RP 100	RP 500
Standard	0%	0%	0%	0%	0%
SSP2-4.5_2050	30%	29%	26%	16%	5%
SSP2-4.5_2100	47%	45%	43%	45%	89%
SSP5-8.5_2050	45%	45%	41%	35%	36%
SSP5-8.5_2100	95%	81%	77%	153%	155%

AAL: average annual loss; RP: return period.

Table 10. Occurrence loss increases in percentage.

	AAL	RP 5	RP 10	RP 100	RP 500
Standard	0%	0%	0%	0%	0%
SSP2-4.5_2050	25%	27%	22%	12%	12%
SSP2-4.5_2100	43%	41%	40%	37%	111%
SSP5-8.5_2050	36%	38%	34%	26%	47%
SSP5-8.5_2100	93%	75%	71%	200%	162%

AAL: average annual loss; RP: return period.

Table 11. Aggregate loss increases in percentage by classification types for SSP5-8.5 scenario in 2100.

Classification Type	Agg/Occ	AAL	RP 5	RP 10	RP 100	RP 500
GD	Aggregate	65%	64%	54%	45%	34%
GX	Aggregate	74%	79%	66%	51%	44%
HN	Aggregate	36%	29%	26%	38%	26%
FZS	Aggregate	164%	134%	145%	288%	265%
JSHL	Aggregate	121%	236%	166%	81%	42%

AAL: average annual loss; RP: return period.

6.3.2. Spatial and Loss Type Analysis

The analysis also reveals significant spatial differences in loss increases, as illustrated for the SSP5-8.5 scenario in 2100 (Table 11). Eastern coastal provinces like Fujian, Zhejiang, and Shanghai are projected to experience much higher percentage increases in total loss compared with southern provinces. This geographic disparity is attributed to a northward shift in TC tracks and greater precipitation increases in these northern regions.

Finally, when considering average annual loss, the percentage increase in aggregate loss (i.e., annual summed event losses) is greater than the increase in occurrence loss (i.e., annual maximum event loss). This difference is due to the projected rise in the total number of TCs making landfall on or bypassing China in both 2050 and 2100.

7. Conclusion and Future Study

This study used a newly developed approach to detect typhoon activity, including tracks and strength, from three GCMs (MRI, EC, and BCC). By comparing the typhoon activity from the GCM historical model results with future model results, we identified the characteristics of change in IPCC-defined SSP2-4.5 and SSP5-8.5 scenarios. Using the change characteristics as the target, we built a resampling approach to generate a climate-conditioned catalog in

the Verisk mainland China typhoon model to simulate the economic impact of future climate on the latest industrial exposure datasets.

7.1. Conclusions

Our comprehensive analysis of WNP TCs under future climate change scenarios (SSP2-4.5 and SSP5-8.5) reveals a complex and evolving threat landscape. While GCM results consistently project a downward trend in the overall annual number of TCs, a more critical finding is the discernible shift toward a higher proportion of stronger TCs. This intensification of individual events is coupled with an increasing trend in the number of TCs making landfall on or bypassing mainland China. This heightened intensity and landfalling frequency are projected to intensify further under higher emission scenarios, progressing steadily over the long-term projection period, which underscores a growing risk despite a potential reduction in overall TC count.

An additional prominent finding from this analysis is a general northward shift in the trajectory of WNP TCs. Future tracks under SSP2-4.5 and SSP5-8.5 are projected to be north of historical tracks, with this northward progression becoming more pronounced over time. This trajectory shift is especially evident in the MRI and EC models and reaches its highest significance under the SSP5-8.5 scenario by 2100. Concurrently, the mean TC landfall point along the mainland China coastline is projected to move northward, a shift that becomes more pronounced in the long-term future.

Beyond changes in frequency and intensity, future projections consistently indicate a general increase in TC-induced precipitation per track. This trend is observed for all TCs within the WNP basin and is particularly pronounced for those tracks impacting mainland China, though the increase is notably more significant over the ocean than over land.

These evolving TC characteristics translate into significant spatial variations in projected precipitation impacts along the mainland China coastline. Specifically, TCs making landfall on or bypassing the southern provinces (Hainan, Guangxi, and Guangdong) are projected to induce greater precipitation compared with those impacting the southeast, east, and north China regions. However, this general pattern exhibits a notable exception: under the SSP5-8.5 scenario by 2100, the southeastern provinces (Fujian, Zhejiang, and Shanghai) are projected to experience a significant increase in TC-induced precipitation, indicating localized intensification of extreme rainfall events in these areas.

From a financial perspective, these climatic shifts are projected to lead to substantially increased losses, particularly at longer return periods. By 2100, losses associated with longer return periods (e.g., 500-year events) are projected to increase much more significantly than those at shorter return periods for both SSP2-4.5 and SSP5-8.5. This disproportionate increase is attributed to the projected rise in Category 4 and 5 TCs, which far outpaces changes in lower-category TCs, with Category 1 TCs decreasing in SSP2-4.5 by 2100. Furthermore, the amplified precipitation in 2100 is a major contributor to these increased losses across all return periods. As evidenced by projections for 2100, TC-induced precipitation per track is expected to increase by 26% in Hainan, Guangdong, and Guangxi under SSP2-4.5 and by a substantial 78% in Fujian, Zhejiang, and Shanghai under SSP5-8.5. Consequently,

from an average annual loss perspective, the increased percentage of aggregate loss is projected to be higher than the increased percentage of occurrence loss, driven by the increased number of TCs making landfall on or bypassing China in both 2050 and 2100.

7.2. Study Limitations and Suggestions for Future Research

In this study we used the current vulnerability of commercial and industry buildings and content (i.e., we assumed that building characteristics and vulnerability do not change over time). Also, the study used the relatively low resolution of CMIP6 datasets. We recommend refining this study when high-resolution datasets covering numerous emission scenarios and long-term periods become available.

GCMs are powerful tools, but their projections come with inherent inconsistency and uncertainty. This is not necessarily a flaw, but a reflection of the climate system's staggering complexity. The primary reasons for differing results include each model's unique structure, mathematical equations, and parameterizations – the approximations used for small-scale processes, which affect TC tracks and intensities estimation. Additionally, given the climate's own chaotic nature, known as internal variability, even identical models can produce different outcomes. Scientists address this challenge by using multimodel ensembles, which combine results from many different GCMs. By analyzing the range of projections, they can identify robust trends where models agree and quantify the uncertainty, providing a probabilistic forecast rather than a single definitive prediction. In future studies, we would include additional GCMs in the typhoon study for more robust results.

In our approach, the costliest typhoon in our standard catalog remains the same in the resampled climate-conditioned catalog. However, it is more likely that the 1-in-10,000 or other extreme events will get more intense over time in the changing climate. This is why we only show the economic impact up to 500 years in this study.

In the scientific and insurance community, there is an ongoing debate about the methodology for this type of study: Should we use the GCM future projecting typhoon activity (say from 2025 to 2100) as historical to span a new stochastic catalog rather than resampling from the current climate catalog? After carefully examining numerous GCM model results (both historical reanalysis and future projections) and comparing them with the historical observations, such as best-track datasets, we found the typhoon activity derived from GCM historical reanalysis is very reliable. However, the quality of typhoon activity derived from future projection model results, even from high-resolution (~25 km) results, does not resemble the complex characteristics of the observed TCs. Therefore, our current approach of deriving characteristic change from historical to future scenarios in the same GCM model is a viable solution until future GCM models are significantly improved.

References

Bengtsson, Lennart, Kevin I. Hodges, Monika Esch, Noel Keenlyside, Luis Kornblueh, Jing-Jia Luo, and Toshio Yamagata. 2007. "How May Tropical Cyclones Change in a Warmer Climate?" *Tellus A: Dynamic Meteorology and Oceanography* 59 (4): 539–561. https://doi.org/10.1111/j.1600-0870.2007.00251.x.

Chen, L., Z. Ma, and J. Fei. 2025. "How Different Is Tropical Cyclone Precipitation Over Land and Ocean?" *npj Climate and Atmospheric Science* 8 (70). https://doi.org/10.1038/s41612-025-00970-9.

Colbert, A. J., B. Soden, and B. P. Kirtman. 2015. "The Impact of Natural and Anthropogenic Climate Change on Western North Pacific Tropical Cyclone Tracks." *Journal of Climate* 28 (5): 1806–23. https://doi.org/10.1175/JCLI-D-14-00100.1.

Döscher, R., M. Acosta, A. Alessandri, et al. 2022. "The EC-Earth3 Earth System Model for the Coupled Model Intercomparison Project 6." *Geoscientific Model Development* 15 (7): 2973–3020. https://doi.org/10.5194/gmd-15-2973-2022.

Durack, P. J. 2015. "Sampling the Physical Ocean in CMIP6 Simulations." CLIVAR Ocean Model Development Panel (OMDP) Committee on CMIP6 Ocean Model Output.

Eyring, V., S. Bony, G. A. Meehl, et al. 2016. "Overview of the Coupled Model Intercomparison Project Phase 6 (CMIP6) Experimental Design and Organization." *Geoscientific Model Development* 9 (5): 1937–58. https://doi.org/10.5194/gmd-9-1937-2016.

Flato, G., J. Marotzke, B. Abiodun, et al. 2013. "Evaluation of Climate Models." In *Climate Change 2013: The Physical Science Basis: Working Group I Contribution to the Fifth Assessment Report of the Intergovernmental Panel on Climate Change*. Edited by T. F. Stocker, et al., 741–866. Cambridge University Press.

Han, Y., M.-Z. Zhang, Z. Xu, and W. Guo. 2021. "Assessing the Performance of 33 CMIP6 Models in Simulating the Large-Scale Environmental Fields of Tropical Cyclones." *Climate Dynamics* 58: 2035–54. https://doi.org/10.1007/s00382-021-05986-4.

Hatsuzuka, Daisuke, Tomonori Sato, Kohei Yoshida, Masayoshi Ishii, and Ryo Mizuta. 2020. "Regional Projection of Tropical-Cyclone-Induced Extreme Precipitation Based on Large Ensemble Simulations." *SOLA* 16: 1–6. https://doi.org/10.2151/sola.2020-005.

Hodges, K., A. Cobb, and P. L. Vidale. 2017. "How Well Are Tropical Cyclones Represented in Reanalysis Datasets?" *Journal of Climate* 30 (14): 5243–64.

Horn, Michael, Kevin Walsh, Ming Zhao, Suzana J. Camargo, Enrico Scoccimarro, Hiroyuki Murakami, Hui Wang, Andrew Ballinger, Arun Kumar, Daniel A. Shaevitz, Jeffrey A. Jonas, and Kazuyoshi Oouchi. 2014. "Tracking Scheme Dependence of Simulated Tropical Cyclone Response to Idealized Climate Simulations." *Journal of Climate* 27 (24): 9197–213. https://doi.org/10.1175/JCLI-D-14-00200.1.

IPCC (Intergovernmental Panel on Climate Change). 2021. *Climate Change 2021: The Physical Science Basis: Working Group I Contribution to the Sixth Assessment Report of the Intergovernmental Panel on Climate Change*. Cambridge University Press.

Jin, Y., X. B. Zhang, J. A. Church, et al. 2021. "Projected Sea Level Changes in the Marginal Seas Near China Based on Dynamical Downscaling." *Journal of Climate* 34 (17): 7037–7055.

Kim, Y., B. Kim, K. Y. Jeong, E. Lee, D. Byun, and Y. Cho. 2021. "Local Sea-Level Rise Caused by Climate Change in the Northwest Pacific Marginal Seas Using Dynamical Downscaling." *Frontiers in Marine Science* 8: 620570. https://doi.org/10.3389/fmars.2021.620570.

Knutson, T. R., J. J. Sirutis, M. Zhao, et al. 2015. "Global Projections of Intense Tropical Cyclone Activity for the Late Twenty-First Century from Dynamical Downscaling of CMIP5/RCP4.5 Scenarios." *Journal of Climate* 28 (18): 7203–24. https://doi.org/10.1175/JCLI-D-15-0129.1.

Lai, Y., X. Gu, L. Wei, et al. 2024. "Slower-Decaying Tropical Cyclones Produce Heavier Precipitation over China." *npj Climate and Atmospheric Science* 7 (1): 99. https://doi.org/10.1038/s41612-024-00655-9.

Liu, K. S., J. C. L. Chan, B. Chong, and H. Wong. 2024. "Projections of Future Tropical Cyclone Landfalling Activity in the East Asia Region." *Tropical Cyclone Research and Review* 13 (4): 328–43. https://doi.org/10.1016/j.tcrr.2024.11.004.

Liu, L., and Y. Wang. 2020. "Trends in Landfalling Tropical Cyclone-Induced Precipitation over China." *Journal of Climate* 33 (6): 2223–35. https://doi.org/10.1175/JCLI-D-19-0693.1.

Lu, X. Q., H. Yu, M. Ying, et al. 2021. "Western North Pacific Tropical Cyclone Database Created by the China Meteorological Administration." *Advances in Atmospheric Sciences* 38 (4): 690–9. https://doi.org/10.1007/s00376-020-0211-7.

Murakami, H., P.-C. Hsu, O. Arakawa, and T. Li. 2014. "Influence of Model Biases on Projected Future Changes in Tropical Cyclone Frequency of Occurrence." *Journal of Climate* 27 (6): 2159–81. https://doi.org/10.1175/JCLI-D-13-00436.1.

Nakamura, Jennifer, Suzana J. Camargo, Adam H. Sobel, Naomi Henderson, Kerry A. Emanuel, Arun Kumar, Timothy E. LaRow, Hiroyuki Murakami, Malcolm J. Roberts, Enrico Scoccimarro, Pier Luigi Vidale, Hui Wang, Michael F. Wehner, and Ming Zhao. 2017. "Western North Pacific Tropical Cyclone Model Tracks in Present and Future Climates." *Journal of Geophysical Research-Atmospheres* 122 (18): 9721–44. https://doi.org/10.1002/2017JD027007.

NASA. n.d. "Understanding Sea Level Vital Signs: Ocean Mass." NASA Sea Level Change. Accessed July 16, 2025, from https://sealevel.nasa.gov/understanding-sea-level/key-indicators/ocean-mass/.

Pérez Bello, A., A. Mailhot, D. Paquin, and D. Paquin-Ricard. 2022. "Temperature-Precipitation Scaling Rates: A Rainfall Event-Based Perspective." *Journal of Geophysical Research: Atmospheres* 127 (24): e2022JD037873. https://doi.org/10.1029/2022JD037873.

Qin, L., L. Zhu, B. Liu, et al. 2024. "Global Expansion of Tropical Cyclone Precipitation Footprint." *Nature Communications* 15 (1): 4824. https://doi.org/10.1038/s41467-024-49115-1.

Roberts, Malcolm John, Joanne Camp, Jon Seddon, Pier Luigi Vidale, Kevin Hodges, Benoit Vanniere, et al. 2020a. "Impact of Model Resolution on Tropical Cyclone Simulation Using the HighResMIP-PRIMAVERA Multimodel Ensemble." *Journal of Climate* 33 (7): 2557–83. https://doi.org/10.1175/JCLI-D-19-0639.1.

Roberts, Malcolm John, Joanne Camp, Jon Seddon, Pier Luigi Vidale, Kevin Hodges, Benoit Vanniere, et al. 2020b. "Projected Future Changes in Tropical Cyclones Using the CMIP6 HighResMIP Multimodel Ensemble." *Geophysical Research Letters* 47 (14): e2020GL088662. https://doi.org/10.1029/2020GL088662.

Shan, K., Y. Lin, P. S. Chu, X. Yu, and F. Song. 2023. "Seasonal Advance of Intense Tropical Cyclones in a Warming Climate." *Nature* 623 (7985): 83–9. https://doi.org/10.1038/s41586-023-06544-0.

Shan, K., and X. Yu. 2021. "Variability of Tropical Cyclone Landfalls in China." *Journal of Climate* 34 (22): 9235–47. https://doi.org/10.1175/jcli-d-21-0031.1.

Sharma, A., J. Pathak, M. Prakash, and J. N. Singh. 2021. "Object Detection Using OpenCV and Python." Paper presented at the Third International Conference on Advances in Computing, Communication Control, and Networking (ICAC3N), IEEE, Greater Noida, India, 2021. https://doi.org/10.1109/ICAC3N53548.2021.9725638.

Tory, K. J., S. S. Chand, R. A. Dare, and J. L. McBride. 2013. "An Assessment of a Model-, Grid-, and Basin-Independent Tropical Cyclone Detection Scheme in Selected CMIP3 Global Climate Models." *Journal of Climate* 26 (15): 5508–22. https://doi.org/10.1175/JCLI-D-12-00511.1.

Trenberth, K. E., A. Dai, R. M. Rasmussen, and D. B. Parsons. 2003. "The Changing Character of Precipitation." *Bulletin of the American Meteorological Society* 84 (9): 1205–18. https://doi.org/10.1175/BAMS-84-9-1205.

Walsh, K. J. E., M. Fiorino, C. W. Landsea, and K. L. McInnes. 2007. "Objectively Determined Resolution-Dependent Threshold Criteria for the Detection of Tropical Cyclones in Climate Models and Reanalyses." *Journal of Climate* 20 (10): 2307–14. https://doi.org/10.1175/JCLI4074.1.

Walsh, K. J. E., J. L. McBride, P. J. Klotzbach, et al. 2016. "Tropical Cyclones and Climate Change." *Wiley Interdisciplinary Reviews: Climate Change* 7 (1): 65–89. https://doi.org/10.1002/wcc.371.

Wang, H., M. Quan, W. Xu, W. Xiang, W. Li, and Y. Jiang. 2023. "Sea Level Rise Projection in China's Coastal and Offshore Areas." *Haiyang Xuebao (Acta Oceanologica Sinica)* 45 (8): 1–10. https://doi.org/10.12284/hyxb2023096.

Wu, T., and Z. Duan. 2023. "A New and Efficient Method for Tropical Cyclone Detection and Tracking in Gridded Datasets." *Weather and Climate Extremes* 42: 100599. https://doi.org/10.1016/j.wace.2023.100599.

Wu, T., R. Yu, Y. Lu, et al. 2021. "BCC-CSM2-HR: A High-Resolution Version of the Beijing Climate Center Climate System Model." *Geoscientific Model Development* 14 (5): 2977–3006. https://doi.org/10.5194/gmd-14-2977-2021.

Xiang, Q., H. Zhao, P. J. Klotzbach, T. Su, C. Wang, and L. Wu. 2025. "Amplified Bimodal Distribution of Western North Pacific Tropical Cyclone Lifetime Maximum Intensity." *Geophysical Research Letters* 52 (1): e2024GL111637. https://doi.org/10.1029/2024GL111637.

Yan, Y., N. Nanding, X. Li, Y. Shi, and B. Chen. 2025. "Assessment and Application of Tropical Cyclone Clustering in the South China Sea." *Scientific Reports* 15 (1): 1762. https://doi.org/10.1038/s41598-024-83872-9.

Ying, M., W. Zhang, H. Yu, et al. 2014. "An Overview of the China Meteorological Administration Tropical Cyclone Database." *Journal of Atmospheric and Oceanic Technology* 31 (2): 287–301. https://doi.org/10.1175/JTECH-D-12-00119.1.

Yukimoto, S., H. Kawai, T. Koshiro, et al. 2019. "The Meteorological Research Institute Earth System Model Version 2.0, MRI-ESM2.0: Description and Basic Evaluation of the Physical Component." *Journal of the Meteorological Society of Japan, Series II* 97 (5): 931–65. https://doi.org/10.2151/jmsj.2019-051.

Zhai, G., W. Xu, P. Su, L. Qin, and X. Liao. 2024. "Characteristics of Precipitation Changes During Tropical Cyclone Processes in China from 1980 to 2019." *Scientific Reports* 14 (1): 13654. https://doi.org/10.1038/s41598-024-64252-9.

Zhang, W., G. Villarini, E. Scoccimarro, M. Roberts, P. L. Vidale, B. Vanniere, L.-P. Caron, D. Putrasahan, C. Roberts, R. Senan, and M.-P. Moine. 2021. "Tropical Cyclone Precipitation in the HighResMIP Atmosphere-Only Experiments of the PRIMAVERA Project." *Climate Dynamics* 57: 253–73. https://doi.org/10.1007/s00382-021-05707-x.

Zheng, M., and C. Wang. 2023. "Interdecadal Changes of Tropical Cyclone Intensity in the South China Sea." *Climate Dynamics* 60 (1–2): 409–25. https://doi.org/10.1007/s00382-022-06305-1.

Appendices

Appendix A. Performance Comparison of TC Detection Algorithms

The performance of the tropical cyclone (TC) detection algorithm employed in this study was evaluated by comparison with two datasets generated by the prevailing OWZ and TRACK methods. Furthermore, the statistical characteristics of all three TC datasets were benchmarked against the CMA best-track data for the WNP basin over the period 2002–2018.

Table A.1. TC detection algorithm performance comparison.

Metrics	CMA Records	OWZ	TRACK	Method in This Study
Annual TC number	22.65	29.47	33.06	23.59
Variation of annual TC number (std)	3.03	4.15	4.37	2.85
Average duration (h)	179.21	228.34	257.90	162.33
Average track length (km)	3,768.37	5,156.59	5,117.96	3,357.00
Average translation speed (km/h)	21.03	23.61	19.97	20.68
Average landfall ratio	0.29	0.22	0.28	0.25
Average duration after landfall (h)	27.68	39.18	50.92	26.16
Average track length after landfall (km)	551.65	1,101.73	1,188.00	560.61
Average translation speed after landfall (km/h)	22.05	25.51	24.95	22.48

Appendix B. Background: IPCC, CMIP, and SSPs

The IPCC's Sixth Assessment Report, released on August 9, 2021, presents five potential future scenarios for the physical science of climate change. These scenarios are based on complex IPCC modeling, which considers the rate at which humans reduce greenhouse gas emissions. However, the IPCC's models also incorporate socioeconomic factors, such as population growth, urbanization, education, land use, and wealth distribution. For instance, the IPCC projects that population increases can lead to higher fossil fuel and water demands, while education can accelerate technological advancements. Deforestation for agriculture also contributes to rising emissions, according to IPCC findings. Each scenario is categorized by its emissions level and corresponding Shared Socioeconomic Pathway (SSP).

Scenario 1: Most Optimistic (1.5°C by 2050) – SSP1-1.9

This scenario depicts the world achieving net-zero global CO2 emissions around 2050. Society transitions to sustainable practices, prioritizing well-being over economic growth. Investments in education and health rise, while inequality decreases. Although extreme

weather events become more frequent, the worst impacts of climate change are averted. This is the only scenario aligning with the Paris Agreement's 1.5°C warming limit, with temperatures peaking at 1.5°C before declining to 1.4°C by century's end.

Scenario 2: Next Best (1.8°C by 2100) – SSP1-2.6

In this scenario, global CO2 emissions are significantly reduced but at a slower pace, reaching net zero after 2050. Socioeconomic shifts toward sustainability resemble those in Scenario 1, but temperatures stabilize at 1.8°C and the radiative forcing is expected to reach 2.6 W/m^2 by century's end.

Scenario 3: Middle of the Road (2.7°C by 2100) – SSP2-4.5

This middle-of-the-road scenario features CO2 emissions hovering near current levels before declining mid-century without reaching net zero by 2100. Socioeconomic factors follow historical trends, with gradual progress toward sustainability and uneven development. Temperatures rise by 2.7°C, and the radiative forcing is expected to reach 4.5 W/m^2 by century's end.

Scenario 4: Dangerous (3.6°C by 2100) – SSP3-7.0

Emissions and temperatures increase steadily in this scenario, with CO2 emissions doubling from current levels by 2100. Countries prioritize national security and food supplies, fostering competition. Average temperatures rise by 3.6°C, and the radiative forcing is expected to reach 7.0 W/m^2 by century's end.

Scenario 5: Avoid at All Costs (4.4°C by 2100) – SSP5-8.5

This worst-case scenario, as outlined by the IPCC, involves a doubling of current CO2 emissions by 2050. Rapid economic growth is fueled by fossil fuels and energy-intensive lifestyles. The IPCC projects average global temperature to soar by 4.4°C, and the radiative forcing is expected to reach 8.5 W/m^2 by 2100.

Summary

While the IPCC cannot predict the most likely scenario, as this depends on factors such as government policies, the report clearly outlines the potential consequences of different pathways. The IPCC's findings indicate that all scenarios involve continued warming for decades, rising sea levels for centuries to millennia, and Arctic ice-free summers within 30 years. The rate of sea-level rise and the severity of weather events will vary based on the chosen path. Accelerating CO2 reduction is crucial, as emphasized by the IPCC, to mitigate the worst impacts of climate change.